PAPER

Check for updates

Designed construction of hierarchical NiCo$_2$S$_4$@polypyrrole core–shell nanosheet arrays as electrode materials for high-performance hybrid supercapacitors†

Shaojie Chen, Yefeng Yang, [iD]* Ziyue Zhan, Jinlei Xie and Jie Xiong*

In this work, we report the design and fabrication of hierarchical NiCo$_2$S$_4$@polypyrrole (PPy) core–shell hybrid nanosheet arrays on Ni foam as a novel battery-type electrode using a facile hydrothermal and electrodeposition strategy. The conductive and electroactive PPy layers are deliberately coated on the backbones of interconnected NiCo$_2$S$_4$ nanosheets to significantly boost the energy storage capacity. The resulting NiCo$_2$S$_4$@PPy hybrid electrode exhibits an enhanced areal capacity (800 μA h cm^{-2} at 5 mA cm^{-2}) and good rate capability. An aqueous hybrid supercapacitor (HSC) device is assembled by employing NiCo$_2$S$_4$@PPy and activated carbon as the positive and negative electrodes, achieving high energy density (60.8 W h kg^{-1} at 200 W kg^{-1}) and high power density (4362 W kg^{-1} at 31 W h kg^{-1}), as well as excellent cycling stability (98.3% retention over 3000 cycles at 20 mA cm^{-2}). Moreover, two HSC devices can easily light 38 LEDs efficiently, demonstrating the great potential of this core–shell hybrid nanostructure toward practical applications in energy storage devices.

1. Introduction

With the fast growth of portable electronics and hybrid/electric vehicles in modern society, there has been a rapidly increasing demand for safe and reliable energy storage systems with both high energy and power densities.[1–4] As we know, lithium-ion batteries and supercapacitors are two paradigm devices in typical energy storage systems. Usually, batteries can store higher energy than supercapacitors due to the intercalation of large numbers of ions into the electrode materials, while supercapacitors can deliver more power than batteries through the fast accumulation of charges on the electrode surface.[5,6] However, till now batteries and supercapacitors have not been capable of providing plenty of energy and good power densities simultaneously, and researchers are trying to develop new energy storage materials and systems to satisfy the ever-growing energy needs. Recently, hybrid supercapacitors (HSCs) have attracted tremendous attention, since they can bridge the gap between conventional batteries and supercapacitors and exhibit many appealing advantages, such as high power density, improved energy density even comparable to the low end of lithium ion batteries, fast rate of charging–discharging, long service life and safety.[7–11] Typically, HSCs are composed of

a battery-type faradaic electrode (*e.g.*, Co$_3$O$_4$,[12–14] NiCo$_2$O$_4$,[15,16] Co(OH)$_2$,[17] NiAl-LDH,[18] Ni$_3$S$_2$,[19] Ni$_x$Co$_{1-x}$Se[20]) and an electrical double-layer capacitor (EDLC) type electrode (such as carbon nanotube,[21] graphene[22] and carbon foam[23]) as the positive and negative electrode, respectively. Hence, it is highly essential to develop novel battery-type electrode materials with outstanding electrochemical properties, which mainly determines the performance of HSC devices.

Among various battery-type electrode materials, NiCo$_2$S$_4$ has intrigued particular research attention owing to the merits of low cost, facile fabrication as well as possessing richer redox reactions and higher electrical conductivity than the single component oxides and sulfides.[24–29] In the past few years, many efforts have been devoted to further boosting the energy storage efficiency of NiCo$_2$S$_4$ by exploring various NiCo$_2$S$_4$-based core–shell nanostructures.[30,31] For example, Xiao *et al.* reported the successful fabrication of NiCo$_2$S$_4$@Co$_x$Ni$_{1-x}$(OH)$_2$ nanotube/nanosheet arrays on carbon fiber papers with an improved areal capacity of 397 μA h cm^{-2} at a current density of 4 mA cm^{-2}, which is about 3 times that of the pristine NiCo$_2$S$_4$.[27] In another work, Fu and co-workers reported that the electrodeposition of ultrathin CoS$_x$ nanosheets on NiCo$_2$S$_4$ nanotube arrays on Ni foam can achieve a high areal capacity of 592.5 μA h cm^{-2} at 5 mA cm^{-2}.[32] Very recently, Niu *et al.* demonstrated the hydrothermal synthesis of NiCo$_2$S$_4$@Ni$_3$V$_2$O$_8$ core/shell hybrid on Ni foam to obtain a high specific capacity of 142 mA h g^{-1} at 1 A g^{-1}.[33] Although notable progress has been made by the researchers, the designed construction of NiCo$_2$S$_4$-based core–

Department of Materials Engineering, Zhejiang Sci-Tech University, Hangzhou 310018, P. R. China. E-mail: yangyf@zstu.edu.cn; jxiong@zstu.edu.cn; Tel: +86-571-8684-3586

shell nanostructures remains challenging, and many of the assembled HSC devices based on these materials still suffer from the less satisfactory electrochemical performance, especially in terms of achieving both high energy and power densities, which largely restricts their wide practical applications.

Herein, we report the design and fabrication of three-dimensional (3D) hierarchical NiCo$_2$S$_4$@polypyrrole (PPy) core–shell hybrid nanosheet arrays (NSAs) on Ni foam as binder- and additive-free electrodes for supercapacitors. The interconnected NiCo$_2$S$_4$ nanosheets were employed as excellent conductive backbones for docking electroactive materials, while the conducting polymer, PPy in this work, was chosen as the shell materials because of its high electrical conductivity (10–100 S cm^{-1}) and fast redox reaction for charge storage.[34,35] As expected, the coating of PPy nanosheets on the surface of NiCo$_2$S$_4$ can not only facilitate the electron transport in the system, but also provide larger surface area with more contribution of capacity from the shell materials. However, to the best of our knowledge, the combination of NiCo$_2$S$_4$ and PPy in an integrated electrode has been rarely reported.[36] In this work, the optimized NiCo$_2$S$_4$@PPy core–shell hybrid NSAs can exhibit a high areal capacity of 800 μA h cm^{-2} at 5 mA cm^{-2}, and a rate capability of 51.7% with current density increased from 5 to 100 mA cm^{-2}. Remarkably, the aqueous HSC device based on this material displays a high areal capacity of 1528 μA h cm^{-2} at 5 mA cm^{-2}, and excellent cycling stability of 98.3% over 3000 cycles at a high current density of 20 mA cm^{-2}. Moreover, the HSC device can achieve a maximum energy density of 60.8 W h kg^{-1} at a power density of 200 W kg^{-1}, and still retain 31 W h kg^{-1} at a high power density of 4362 W kg^{-1}, suggesting the great potential of this hybrid electrode for high-performance energy storage devices.

2. Experimental section

2.1 Preparation of NiCo$_2$S$_4$ NSAs on Ni foam

All chemicals were purchased from Shanghai Sinopharm Chemical Reagents and used without further purification. The high-quality NiCo$_2$S$_4$ NSAs were fabricated *via* a facile hydrothermal process followed by an ion exchange reaction. Briefly, a mixed solution containing 1 mmol Ni(NO$_3$)$_2$·6H$_2$O, 2 mmol Co(NO$_3$)$_2$·6H$_2$O, 12 mmol urea, and 6 mmol NH$_4$F in 80 mL distilled water was transferred into a 100 mL Teflon-lined stainless steel autoclave, with a piece of Ni foam as the substrate. Then, the autoclave was sealed and kept at 120 °C for 1 h. In the chemical reaction, Co^{2+} and Ni^{2+} ions first reacted with the hydrolysis product of urea to form the Ni–Co carbonate hydroxide precursors. The resulting Ni–Co precursor NSAs on Ni foam were collected and further thermally converted into desired NiCo$_2$S$_4$ NSAs through an anion exchange reaction with S^{2-} ions released by Na$_2$S aqueous solution at 120 °C. The final products were rinsed with distilled water and ethanol successively, and dried in air overnight.

2.2 Preparation of NiCo$_2$S$_4$@PPy core–shell NSAs

The growth of PPy on the surface of NiCo$_2$S$_4$ NSAs was conducted by an electrodeposition method in a standard three-electrode cell on an electrochemical workstation (CHI760E). The Ni foam loaded with NiCo$_2$S$_4$ was directly utilized as the working electrode, while Pt foil and saturated calomel electrode (SCE) were used as the counter electrode and reference electrode, respectively. Prior to the reaction, the NiCo$_2$S$_4$ NSAs on Ni foam were immersed into an aqueous solution containing LiClO$_4$ (0.3 M) and pyrrole (0.5 M) for 1 h. Afterwards, electrochemical polymerization of pyrrole monomer was performed by an electrochemical oxidation process under a constant voltage of 0.8 V (*vs.* SCE) for 5 min at room temperature. Eventually, the obtained NiCo$_2$S$_4$@PPy core–shell hybrid electrode was rinsed with water and ethanol for several times and dried at 80 °C in air overnight. The mass loading of PPy is calculated to be *ca.* 2.4 mg cm^{-2}, and the total mass loading of the NiCo$_2$S$_4$@PPy is *ca.* 4.3 mg cm^{-2}. For comparison, pure PPy on Ni foam was also prepared in a similar procedure by electrodeposition.

2.3 Fabrication of aqueous hybrid supercapacitors (HSCs)

The HSC devices were constructed by integrating the NiCo$_2$S$_4$@PPy and activated carbon (AC) as the positive and negative electrodes, respectively. The two electrodes were separated by a piece of porous cellulose paper in 2 M KOH aqueous electrolyte, and pressed together in a CR-2025 coin cell (denoted as NiCo$_2$S$_4$@PPy//AC). Specifically, the mass of active materials on the positive and negative electrodes were carefully matched by balancing the charges stored in both electrodes with $Q_+ = Q_-$.

2.4 Materials characterization

The crystalline structure of the products was characterized by X-ray diffraction (XRD) on a Bruker D8 Advance diffractometer with Cu Kα radiation ($\lambda = 1.5406$ Å). The morphology and microstructure of the products were investigated by field-emission scanning electron microscopy (FE-SEM, Hitachi S4800) and high-resolution transmission electron microscopy (HRTEM, FEI Tecnai F20), respectively. The elemental compositions were analyzed by energy-dispersive X-ray spectroscopy (EDS) with a high-angle annular dark-field (HAADF) detector under scanning TEM (STEM) mode on Tecnai F20. The Fourier transform infrared (FTIR) spectra were obtained on a Nicolet 5700 spectrometer.

2.5 Electrochemical measurements

All the cyclic voltammetry (CV), galvanostatic charge–discharge and electrochemical impedance spectroscopy (EIS) tests were conducted on an electrochemical workstation (CHI760E) in 2 M KOH aqueous solution. For single electrodes, the electrochemical measurements were carried out in a three-electrode configuration, with Pt foil and SCE acting as the counter and reference electrodes, respectively. Regarding the full-cell devices, the electrochemical properties were explored in a two-electrode configuration with the NiCo$_2$S$_4$@PPy as the positive electrode and AC as the negative electrode, respectively.

The areal capacities for the battery-type electrodes were determined based on the following equation:

$$Q_a = It/S$$

where Q_a (μA h cm^{-2}) is the areal capacity, I (A) is the discharge current, t (s) is the discharge time, S (cm^2) is the geometrical area of the electrode.

The specific energy and power densities of the HSC devices were derived based on the total mass of active materials on both electrodes according to the following equations:[37]

$$E = \frac{I \int_{t(U_{max})}^{t(U_{min})} U(t)\mathrm{d}t}{m}$$

$$P = E/t$$

where E (W h kg^{-1}) is the energy density, P (W kg^{-1}) is the power density, m (g) is the total mass of active materials on both electrodes, I (A) is the discharge current, U (V) is the potential of the device and t (s) is the discharge time from the discharge curve, respectively.

3. Results and discussion

In this work, we present a facile strategy to fabricate the unique 3D NiCo$_2$S$_4$@PPy core–shell hybrid NSAs on conductive substrates, which mainly involves two key steps as schematically illustrated in Fig. 1. Firstly, the high-quality NiCo$_2$S$_4$ NSAs were grown on Ni foam through a hydrothermal method followed by an ion-exchange reaction of S^{2-} ions in the solution. In the next step, sheet-like PPy conductive layers were cross-linked from Py monomers and deposited on the surface of NiCo$_2$S$_4$ backbones *via* an electrochemical polymerization process, which successfully resulted in the formation of 3D hierarchical NiCo$_2$S$_4$@PPy core–shell nanostructures. We are able to control the coating of PPy layers with different amounts by simply adjusting the electrodeposition time, as demonstrated by the SEM images in Fig. S1.† In this work, we will mainly focus on the NiCo$_2$S$_4$@PPy electrode with PPy layers coated by 5 min, which has the optimized electrochemical properties. It should be mentioned that prior to the polymerization process, sufficient Py monomers were deliberately adsorbed on the surface of NiCo$_2$S$_4$ in the electrolyte to facilitate the polymerization process and protect the NiCo$_2$S$_4$ backbones from oxidation.

The crystalline structure and phase purity of the hybrid composite were probed by XRD measurement. Fig. 2 shows the typical XRD pattern of the NiCo$_2$S$_4$@PPy hybrid NSAs on Ni foam substrate. The diffraction peaks at 2θ values of $31.6°$, $38.3°$, $47.4°$, $50.5°$ and $55.4°$ can be readily identified as the
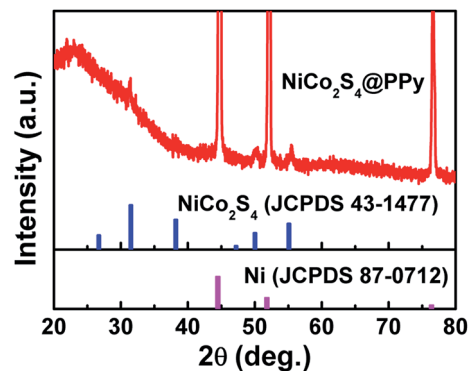

Fig. 2 Typical XRD pattern of the NiCo$_2$S$_4$@PPy hybrid NSAs on Ni foam substrate.

(311), (400), (422), (511) and (440) planes of the NiCo$_2$S$_4$ phase (JCPDS no. 43-1477), while the three dominant peaks at $44.7°$, $52.1°$ and $76.5°$ are attributed to the Ni foam substrate (JCPDS no. 87-0712).[38] Apart from these peaks, a broad peak centered at *ca.* $23°$ arising from the coated PPy phase is also detected, which is distinctly in agreement with the reported literatures on PPy-based composites,[39–41] reflecting the poor crystallinity of the PPy layers within the hybrid composite.

The surface morphologies of the products were characterized by FESEM. For the pristine NiCo$_2$S$_4$ (Fig. 3A and B), it is revealed that the whole Ni foam skeleton has been covered by high-density of NiCo$_2$S$_4$ nanosheets with an average wall thickness of *ca.* 50 nm and lateral size ranging from 1 to 2 μm. These NiCo$_2$S$_4$ nanosheets directly grown on Ni foam are observed to interconnect with each other to form a 3D porous network with adequate interspaces among them, which can be utilized as ideal conductive backbones to support additional electroactive materials. After the electrodeposition, as shown in Fig. 3C and D, one can see that the NiCo$_2$S$_4$ backbones have been entirely wrapped by a thin film of PPy shell materials with total thickness increased to *ca.* 120 nm, forming the desirable hierarchical NiCo$_2$S$_4$@PPy core–shell hybrid nanostructures. Despite the integration of PPy into the composite, the array structures are well retained. Moreover, high-magnification SEM image (Fig. S2†) indicates that the PPy shell materials are in fact composed of many tiny nanosheets, which can be further confirmed by TEM.

Further insights into the morphology and microstructure of the products were revealed by TEM and HRTEM. Fig. 4A shows a typical TEM image of an individual NiCo$_2$S$_4$ nanosheet with relatively smooth surface. More details are clearly illustrated by HRTEM. As shown in Fig. S3,† the NiCo$_2$S$_4$ nanosheets are observed to possess many crystalline particles and mesopores in them, demonstrating their polycrystalline characteristics. The HRTEM image in Fig. 4B exhibits two sets of visible lattice fringes with an interplanar spacing of 0.34 and 0.28 nm, corresponding well to the (220) and (311) planes of cubic NiCo$_2$S$_4$ phase, respectively, as supported by previously reported literatures on NiCo$_2$S$_4$.[26,42] The TEM image taken from the NiCo$_2$S$_4$@PPy hybrid NSAs (Fig. 4C) confirms that the surface of NiCo$_2$S$_4$ nanosheet has been successfully deposited with a layer
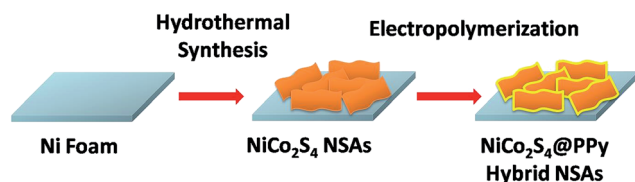

Fig. 1 Schematic illustration of the synthetic procedure for NiCo$_2$S$_4$@PPy core–shell hybrid NSAs on Ni foam.
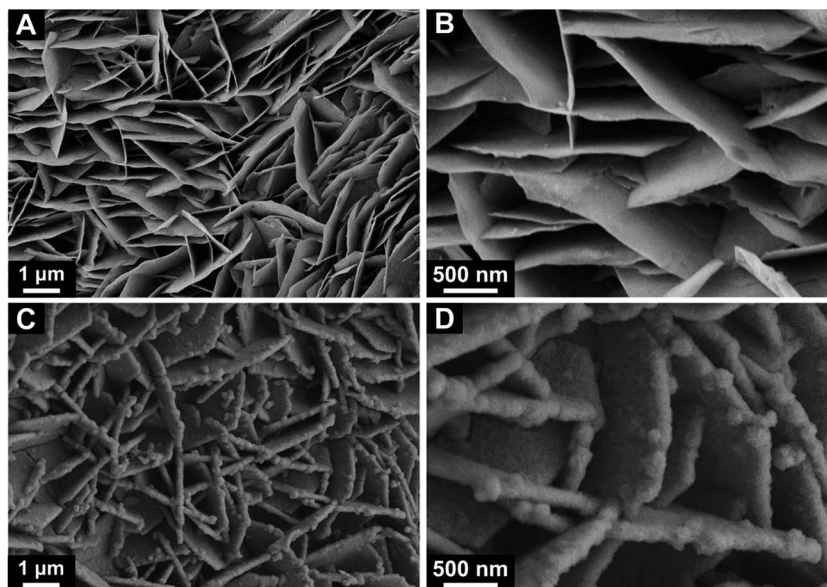
Fig. 3 Typical SEM images of (A and B) pristine NiCo$_2$S$_4$ and (C and D) NiCo$_2$S$_4$@PPy hybrid NSAs at low- and high-magnification, respectively.

of ultrathin and interconnected PPy nanosheets, which can provide more electroactive sites and greatly facilitate the charge transfer in the system to boost the energy storage efficiency. HRTEM studies (Fig. 4D) reveal the distinct interface between the NiCo$_2$S$_4$ core and amorphous PPy shells with a layer thickness of *ca.* 30 nm, unambiguously testifying the core–shell heterostructures. In addition, the EDS mapping analysis by HAADF-STEM (Fig. 5) shows that the constituent elements of C,
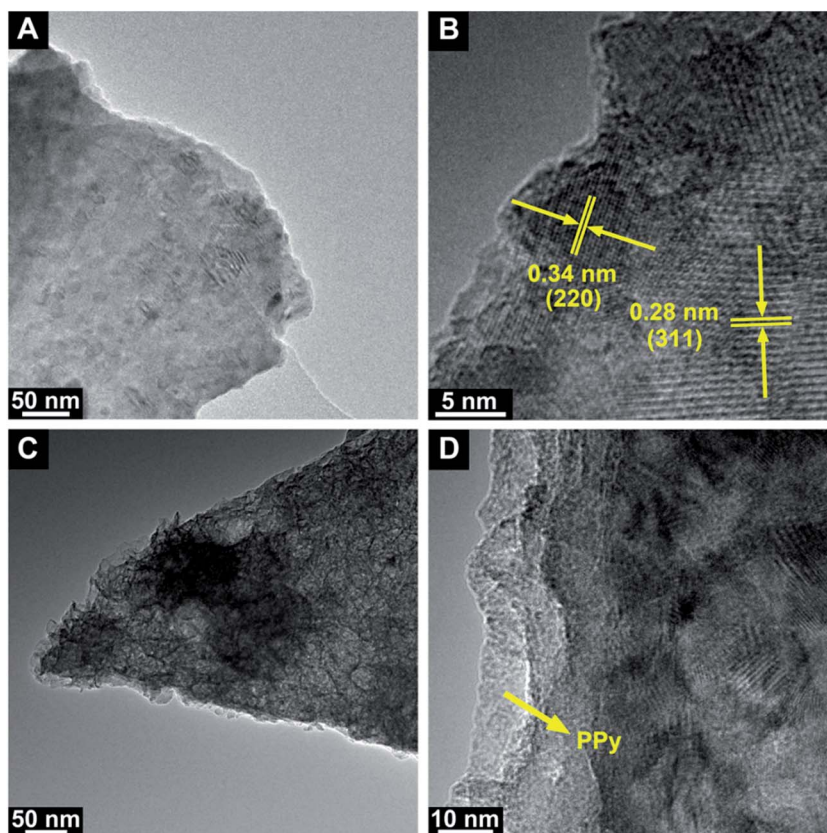

Fig. 4 (A) TEM and (B) HRTEM images of an individual NiCo$_2$S$_4$ nanosheet, (C) TEM image of NiCo$_2$S$_4$@PPy hybrid nanosheet, and (D) corresponding HRTEM image revealing the PPy thin layers coated on the surface of NiCo$_2$S$_4$.
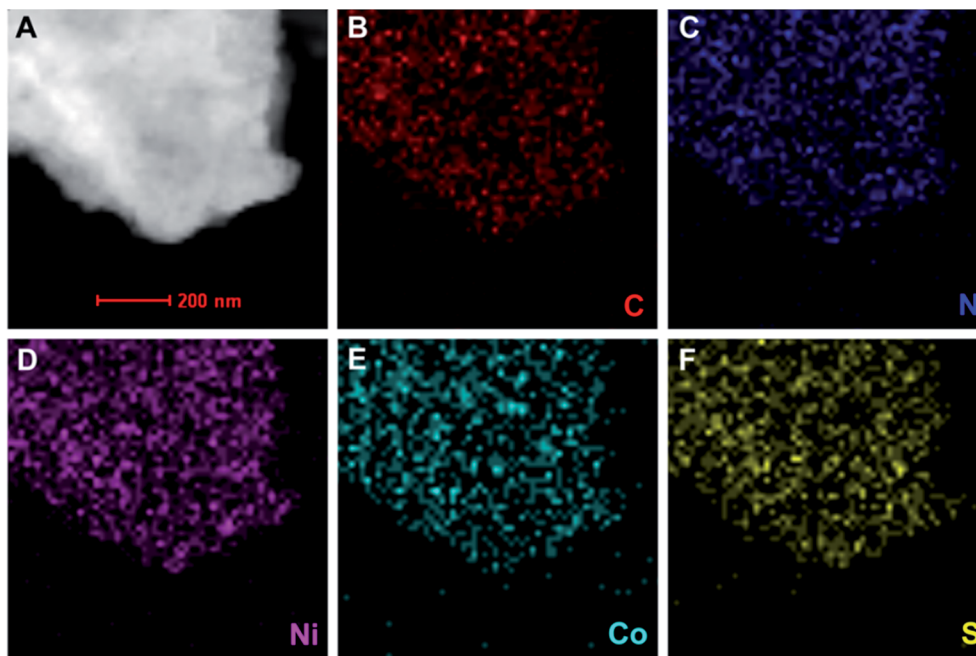
Fig. 5 (A) Typical HAADF-STEM image of an individual $NiCo_2S_4$@PPy hybrid nanosheet, and (B–F) corresponding EDS mapping analysis.

N, Ni, Co and S can be detected throughout the observed nanosheet region, suggesting the homogenous distribution of PPy shell materials on the whole $NiCo_2S_4$ backbones, which is consistent with TEM measurement. Moreover, FTIR has been utilized to explore the functional organic groups from PPy layers, and the result is illustrated in Fig. S4,† which clearly demonstrates the successful coating of PPy layers on the $NiCo_2S_4$ nanosheets.

The superior electrochemical properties of hierarchical $NiCo_2S_4$@PPy core–shell hybrid NSAs for supercapacitors were first investigated in a three-electrode system with 2 M KOH solution as the electrolyte. The CV curves of the pristine $NiCo_2S_4$, PPy and $NiCo_2S_4$@PPy hybrid electrodes as well as bare Ni foam were tested at a scan rate of 10 mV s^{-1} with a potential window ranging from -0.1 to 0.6 V, as shown in Fig. 6A and S5.† It should be pointed out that the contribution of Ni foam substrate to the overall capacity can be neglected since there is almost no evident redox peaks from Ni foam. For the pristine $NiCo_2S_4$, a pair of broad peaks arising from the redox reactions of $NiCo_2S_4$ in alkaline solution is visible, suggesting the faradaic characteristics of battery-type electrodes,[8,43] which is quite different from the EDLC-type and pseudocapacitive such as MnO_2 (ref. 44) and RuO_2 (ref. 45) electrodes with nearly rect-angular CV shapes. The mechanism of the electrochemical reaction can be attributed to the faradaic redox process of Co^{2+}/Co^{3+}/Co^{4+} and Ni^{2+}/Ni^{3+} based on the following equations:[36,42] $NiCo_2S_4 + OH^- + H_2O \leftrightarrow NiSOH + 2CoSOH + 2e^-$, $CoSOH + OH^- \leftrightarrow CoSO + H_2O + e^-$. After the coating of PPy nanosheets, the PPy shells are able to contribute additional capacity via doping/de-doping in alkaline solution.[46] As expected, the $NiCo_2S_4$@PPy hybrid electrode exhibits much increased CV integrated area than the pristine $NiCo_2S_4$ and PPy electrodes, indicating the

largely enhanced energy storage capacity for the hybrid elec-trode.[47] Fig. 6B compares the galvanostatic discharge curves of these electrodes at the same current density of 10 mA cm^{-2}. As observed, the $NiCo_2S_4$@PPy hybrid electrode displays a much longer discharging time than the other electrodes, further demonstrating the improved electrochemical performance of the hybrid electrode through PPy coating. Fig. 6C displays the CV curves of the $NiCo_2S_4$@PPy hybrid electrode recorded at various scan rates ranging from 2 to 20 mV s^{-1}. The shapes of these CV curves show no significant changes as the scan rate increases, suggesting that this hybrid electrode is favorable for high-rate energy storage process.[48] Fig. 6D presents the galvanostatic discharge curves of the $NiCo_2S_4$@PPy hybrid electrode at different current densities varying from 5 to 100 mA cm^{-2}. The areal capacities of the $NiCo_2S_4$@PPy hybrid electrode are calcu-lated from the discharge curves and plotted as a function of current density in Fig. 6E with pristine $NiCo_2S_4$ and PPy also included for comparison. Within the whole current density range, the $NiCo_2S_4$@PPy hybrid electrode delivers a much higher areal capacity than that of pristine $NiCo_2S_4$ and PPy (the areal capacity of PPy rapidly decreases to zero at a current density of 30 mA cm^{-2}). Remarkably, the $NiCo_2S_4$@PPy hybrid electrode displays a high areal capacity of 800 μA h cm^{-2} at a current density of 5 mA cm^{-2}, which is about 2.1 times that of pristine $NiCo_2S_4$ (383.9 μA h cm^{-2}) and nearly 74 times that of PPy (10.8 μA h cm^{-2}) under the same condition. This result is also much higher than those reported values on core–shell electrodes on Ni foam, such as $NiCo_2O_4$@$NiCo_2O_4$,[15] $NiCo_2S_4$@MnO_2,[31] $ZnCo_2O_4$@PPy,[39] $NiCo_2O_4$@PPy,[41] $NiCo_2O_4$@PEDOT,[46] $NiCo_2S_4$@$Ni(OH)_2$,[49] $NiMoO_4$@$Co(OH)_2$,[50] $NiCo_2O_4$@$Co_xNi_{1-x}(OH)_2$.[51] Moreover, even at a current density as high as 100 mA cm^{-2}, the $NiCo_2S_4$@PPy hybrid electrode still manifests a high areal
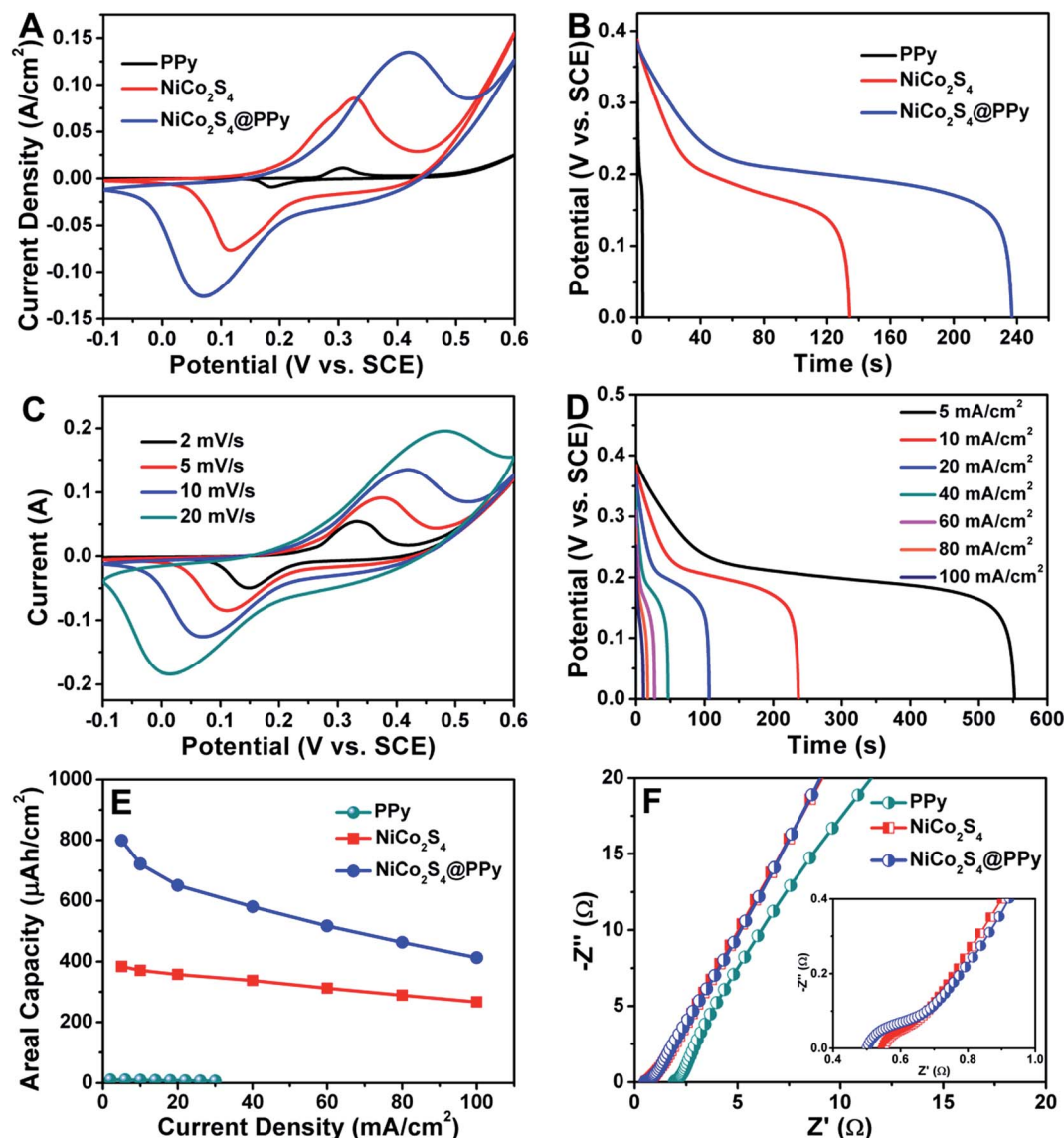
Fig. 6 (A) CV curves of the NiCo$_2$S$_4$@PPy, NiCo$_2$S$_4$ and PPy electrodes at a scan rate of 10 mV s^{-1}, (B) discharge curves of the NiCo$_2$S$_4$@PPy, NiCo$_2$S$_4$ and PPy electrodes at a current density of 10 mA cm^{-2}, (C) CV curves of the NiCo$_2$S$_4$@PPy electrode at various scan rates, (D) discharge curves of the NiCo$_2$S$_4$@PPy electrode at different current densities, (E) areal capacities of the NiCo$_2$S$_4$@PPy, NiCo$_2$S$_4$ and PPy electrodes as a function of current density, and (F) Nyquist plots of the NiCo$_2$S$_4$@PPy, NiCo$_2$S$_4$ and PPy electrodes, inset showing the magnification part of high frequency range.

capacity of 413 μA h cm^{-2} with 51.7% retention of the initial capacity, which is about 1.6 times that of pristine NiCo$_2$S$_4$ (265 μA h cm^{-2}). The enhanced electrochemical properties for the hybrid electrode can be explained by the integration of NiCo$_2$S$_4$ and PPy in such a unique hierarchical structure as well as the distinct synergetic contribution from the core–shell components.

To further understand the superior electrochemical performance of the NiCo$_2$S$_4$@PPy hybrid electrode, EIS measurements were carried out in a frequency range of 0.01 Hz to 100 kHz. Fig. 6F presents the Nyquist plots of pristine NiCo$_2$S$_4$, PPy and NiCo$_2$S$_4$@PPy hybrid electrodes. In the high frequency region, the real axis intercept of the curve indicates the bulk resistance, and the semicircle diameter reflects the charge transfer resistance, while in the low frequency region, the straight slope of

the curve shows the Warburg resistance (ion diffusion resistance).[52,53] As shown in Fig. 6F, the NiCo$_2$S$_4$@PPy hybrid electrode exhibits a decreased bulk resistance than that of pristine NiCo$_2$S$_4$ and PPy and a minimized charge transfer resistance, suggesting the improved electrical conductivity of NiCo$_2$S$_4$ through the coating of PPy layers. Besides, the very similar slope of straight line for these electrodes implies that the interconnected core–shell nanostructures are highly accessible for ion diffusion into the electrodes. Owing to the fast electron transport and facile ion diffusion kinetics, the designed formation of NiCo$_2$S$_4$@PPy hybrid NSAs shall hold great promise as electrodes for high-performance HSCs.

To evaluate the electrochemical performance of the NiCo$_2$S$_4$@PPy hybrid NSAs in real devices, an aqueous HSC device was
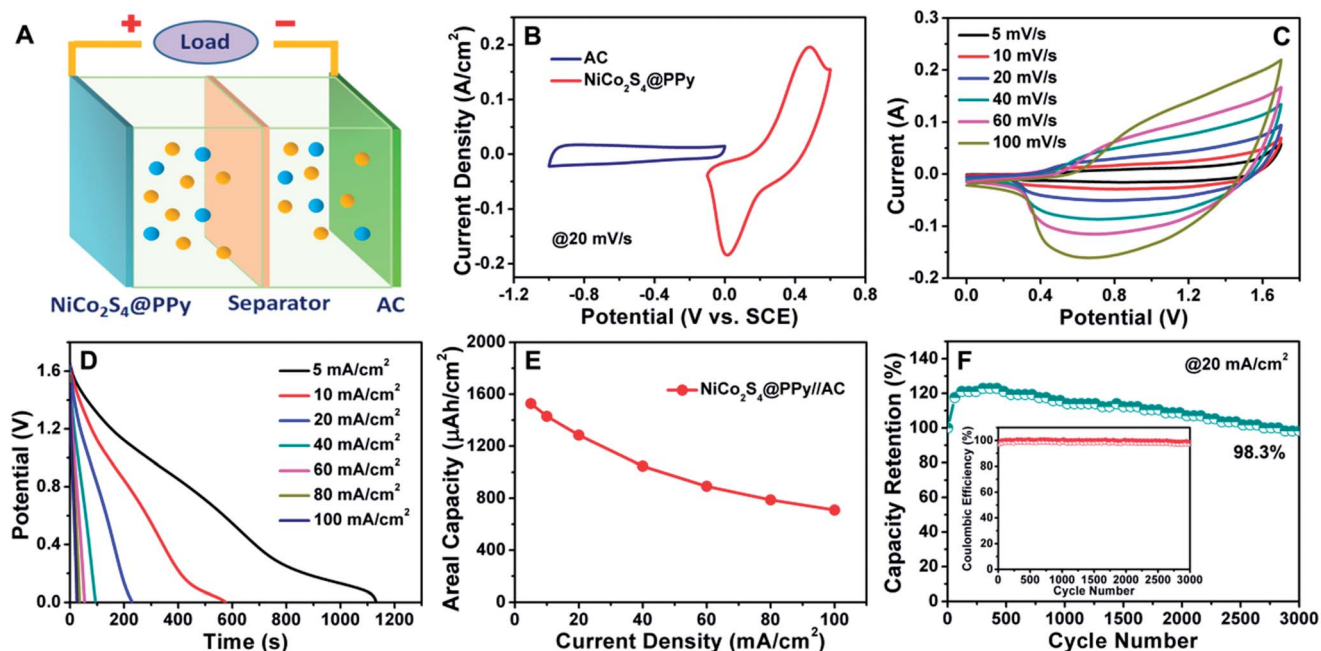
Fig. 7 (A) Schematic illustration of the HSC device configuration, (B) CV curves of the NiCo$_2$S$_4$@PPy and AC electrodes at the same scan rate of 20 mV s^{-1}, (C) CV and (D) discharge curves of the NiCo$_2$S$_4$@PPy//AC device, (E) rate capability of the NiCo$_2$S$_4$@PPy//AC device, (F) cycling stability of the NiCo$_2$S$_4$@PPy//AC device over 3000 cycles at 20 mA cm^{-2}, inset showing the variation of the coulombic efficiency during the cycling process.

fabricated by employing the NiCo$_2$S$_4$@PPy and AC as the positive and negative electrodes, respectively, as schematically illustrated in Fig. 7A. The CV curves of the NiCo$_2$S$_4$@PPy and AC electrodes were first investigated in a three-electrode system (Fig. 7B) with a voltage window of −0.1 to 0.6 V and −1.0 to 0 V, respectively. It can be thus inferred that the as-fabricated NiCo$_2$S$_4$@PPy//AC HSC device is capable of affording a stable operating voltage of 1.7 V. Fig. 8C shows the CV curves of the NiCo$_2$S$_4$@PPy//AC device recorded at various scan rates from 5 to 100 mV s^{-1}, which reveals the combined contribution of a battery-type faradaic electrode and a capacitor-type electrode to the CV behaviors. Fig. 7D displays the galvanostatic discharge curves of the device under different current densities ranging from 5 to 100 mA cm^{-2}. The NiCo$_2$S$_4$@PPy//AC HSC device delivers an areal capacity of

1528 µA h cm^{-2} at 5 mA cm^{-2}, and still retains 710 µA h cm^{-2} at a high current density of 100 mA cm^{-2}, as illustrated in Fig. 7E. The cycling stability of the HSC device is very important and also evaluated by repeated charge–discharge tests at 20 mA cm^{-2}. As shown in Fig. 7F, the overall areal capacity of the device increases at the beginning of several hundred cycles due to the slow activation of the electrode materials, and then gradually decays with increasing cycles. After 3000 cycles, the HSC device still exhibits 98.3% retention of the initial value and nearly 100% coulombic efficiency, demonstrating the outstanding long-term cycling stability and good electrochemical reversibility. This fact can be also reflected by the SEM image of NiCo$_2$S$_4$@PPy electrode of the HSC device after 3000 cycles, with slightly changed morphology and structure as shown in Fig. S6.†

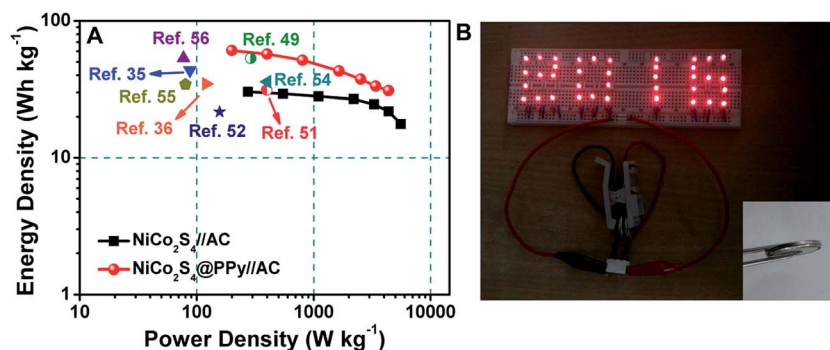Fig. 8 (A) Ragone plots of the NiCo$_2$S$_4$@PPy//AC and NiCo$_2$S$_4$//AC HSC devices, as compared with the values of other reported devices in literature; (B) a photograph of 38 red LEDS driven by two HSC devices connected in series, showing the bright characters of "2016", inset showing the photograph of assembled coin-cell device.

The energy density and power density are two vital parameters generally used to evaluate the energy storage devices for practical applications. Fig. 8A displays the Ragone plots of as-fabricated $NiCo_2S_4@PPy//AC$ and $NiCo_2S_4//AC$ devices, and data of some previously reported devices in aqueous electrolyte are also provided for comparison. It is worth noting that the $NiCo_2S_4@PPy//AC$ device achieves a maximum energy density of 60.8 W h kg^{-1} at a power density of 200 W kg^{-1}, and is still capable of retaining 31 W h kg^{-1} even at a high power density of 4362 W kg^{-1}, which is about 2 times that of $NiCo_2S_4//AC$ (30.3 W h kg^{-1} at 274 W kg^{-1}, and 17.7 W h kg^{-1} at 5554 W kg^{-1}). Notably, the obtained energy density of the $NiCo_2S_4@PPy//AC$ device is comparable or even superior to many of the recently reported aqueous HSC devices, such as CoO@PPy/AC (43.5 W h kg^{-1} at 87.5 W kg^{-1}),[35] $NiCo_2S_4@PPy//AC$ (34.6 W h kg^{-1} at 120.2 W kg^{-1}),[36] $NiCo_2S_4@Ni(OH)_2//AC$ (53.3 W h kg^{-1} at 290 W kg^{-1}),[49] $NiCo_2O_4@Co_xNi_{1-x}(OH)_2//CMK-3$ (31.2 W h kg^{-1} at 396 W kg^{-1}),[51] $NiCo_2O_4@NiMoO_4//AC$ (21.7 W h kg^{-1} at 157 W kg^{-1}),[52] $NiCo_2S_4@Co(OH)_2//AC$ (35.9 W h kg^{-1} at 400 W kg^{-1}),[54] $Co_3O_4@PPy@MnO_2//AC$ (34.3 W h kg^{-1} at 80 W kg^{-1})[55] and $TiO_2@Ni(OH)_2//$mesoporous carbon (53.5 W h kg^{-1} at 77.1 W kg^{-1}).[56] To further highlight the high energy and high power performance, two $NiCo_2S_4@PPy//AC$ devices are assembled in CR-2025 coin cells and connected in series. As shown in Fig. 8B, the devices can easily power 38 red LEDs with the characters of "2016" brightly after a short time of charging, strongly suggesting the great potential in practical applications as advanced energy storage devices.

4.   Conclusion

In summary, a 3D core–shell heterostructure of $NiCo_2S_4@PPy$ NSAs was rationally designed and fabricated on Ni foam through a facile multi-step synthetic approach. With the integration of $NiCo_2S_4$ nanosheets and PPy layers as the core and shell materials, the optimized hybrid electrode can deliver an enhanced areal capacity of 800 µA h cm^{-2} at 5 mA cm^{-2} and a reasonably high rate capability with current density increased by 20 times. Moreover, an aqueous HSC device based on $NiCo_2S_4@PPy$ NSAs is assembled, demonstrating the high energy density (60.8 W h kg^{-1} at 200 W kg^{-1}), high power density (4362 W kg^{-1} at 31 W h kg^{-1}) and outstanding long-term cycling stability (98.3% retention over 3000 cycles) for the device. Our work provide an effective strategy toward developing high-performance battery-type electrodes for supercapacitors by engineering $NiCo_2S_4$ and PPy in a unique core–shell structure, and the resulting hybrid nanostructure shall have great promise in advanced energy storage devices as electrode materials.

Acknowledgements

References

1   P. Simon and Y. Gogotsi, *Nat. Mater.*, 2008, **7**, 845–854.
2   W. Li, L. P. Xin, X. Xu, Q. D. Liu, M. Zhang, S. J. Ding, M. S. Zhao and X. J. Lou, *Sci. Rep.*, 2015, **5**, 9277.
3   W. Hu, R. Q. Chen, W. Xie, L. L. Zou, N. Qin and D. H. Bao, *ACS Appl. Mater. Interfaces*, 2014, **6**, 19318–19326.
4   J. P. Liu, J. Jiang, C. W. Cheng, H. X. Li, J. X. Zhang, H. Gong and H. J. Fan, *Adv. Mater.*, 2011, **23**, 2076–2081.
5   W. H. Zuo, C. Wang, Y. Y. Li and J. P. Liu, *Sci. Rep.*, 2015, **5**, 7780.
6   Y. Jiao, J. Pei, C. S. Yan, D. H. Chen, Y. Y. Hu and G. Chen, *J. Mater. Chem. A*, 2016, **4**, 13344–13351.
7   D. P. Dubal, O. Ayyad, V. Ruiz and P. Gomez-Romero, *Chem. Soc. Rev.*, 2015, **44**, 1777–1790.
8   T. W. Lin, M. C. Hsiao, S. W. Chou, H. H. Shen and J. Y. Lin, *J. Electrochem. Soc.*, 2015, **162**, A1493–A1499.
9   H. Kim, M.-Y. Cho, M.-H. Kim, K.-Y. Park, H. Gwon, Y. Lee, K. C. Roh and K. Kang, *Adv. Energy Mater.*, 2013, **3**, 1500–1506.
10 R. Z. Li, Y. M. Wang, C. Zhou, C. Wang, X. Ba, Y. Y. Li, X. T. Huang and J. P. Liu, *Adv. Funct. Mater.*, 2015, **25**, 5384–5394.
11 W. B. Fu, Y. L. Wang, W. H. Han, Z. M. Zhang, H. M. Zha and E. Q. Xie, *J. Mater. Chem. A*, 2016, **4**, 173–182.
12 Y. F. Yuan, X. H. Xia, J. B. Wu, X. H. Huang, Y. B. Pei, J. L. Yang and S. Y. Guo, *Electrochem. Commun.*, 2011, **13**, 1123–1126.
13 G. H. Zhang, T. H. Wang, X. Z. Yu, H. N. Zhang, H. G. Duan and B. A. Lu, *Nano Energy*, 2013, **2**, 586–594.
14 Q. Yang, Z. Y. Lu, X. M. Sun and J. F. Liu, *Sci. Rep.*, 2013, **3**, 3537.
15 X. Y. Liu, S. J. Shi, Q. Q. Xiong, L. Li, Y. J. Zhang, H. Tang, C. D. Gu, X. L. Wang and J. P. Tu, *ACS Appl. Mater. Interfaces*, 2013, **5**, 8790–8795.
16 L. Huang, D. C. Chen, Y. Ding, S. Feng, Z. L. Wang and M. L. Liu, *Nano Lett.*, 2013, **13**, 3135–3139.
17 R. T. Wang, X. B. Yan, J. W. Lang, Z. M. Zheng and P. Zhang, *J. Mater. Chem. A*, 2014, **2**, 12724–12732.
18 M. Li, F. Liu, J. P. Cheng, J. Ying and X. B. Zhang, *J. Alloys Compd.*, 2015, **635**, 225–232.
19 C. S. Dai, P. Y. Chien, J. Y. Lin, S. W. Chou, W. K. Wu, P. H. Li, K. Y. Wu and T. W. Lin, *ACS Appl. Mater. Interfaces*, 2013, **5**, 12168–12174.
20 H. Chen, S. Chen, M. Fan, C. Li, D. Chen, G. Tian and K. Shu, *J. Mater. Chem. A*, 2015, **3**, 23653–23659.
21 B. S. Mao, Z. H. Wen, Z. Bo, J. B. Chang, X. K. Huang and J. H. Chen, *ACS Appl. Mater. Interfaces*, 2014, **6**, 9881–9889.
22 L. L. Zhang, X. Zhao, M. D. Stoller, Y. W. Zhu, H. X. Ji, S. Murali, Y. P. Wu, S. Perales, B. Clevenger and R. S. Ruoff, *Nano Lett.*, 2012, **12**, 1806–1812.

23 B. You, J. H. Jiang and S. J. Fan, *ACS Appl. Mater. Interfaces*, 2014, **6**, 15302–15308.

24 X. M. Li, Q. G. Li, Y. Wu, M. C. Rui and H. B. Zeng, *ACS Appl. Mater. Interfaces*, 2015, **7**, 19316–19323.

25 L. F. Shen, L. Yu, H. B. Wu, X. Y. Yu, X. G. Zhang and X. W. Lou, *Nat. Commun.*, 2015, **6**, 6694.

26 H. C. Chen, J. J. Jiang, L. Zhang, D. D. Xia, Y. D. Zhao, D. Q. Guo, T. Qi and H. Z. Wan, *J. Power Sources*, 2014, **254**, 249–257.

27 J. W. Xiao, L. Wan, S. H. Yang, F. Xiao and S. Wang, *Nano Lett.*, 2014, **14**, 831–838.

28 R. Zou, Z. Zhang, M. F. Yuen, M. Sun, J. Hu, C.-S. Lee and W. Zhang, *NPG Asia Mater.*, 2015, **7**, e195.

29 R. Zou, M. F. Yuen, L. Yu, J. Hu, C.-S. Lee and W. Zhang, *Sci. Rep.*, 2016, **6**, 20264.

30 H. Z. Wan, J. Liu, Y. J. Ruan, L. Lv, L. Peng, X. Ji, L. Miao and J. J. Jiang, *ACS Appl. Mater. Interfaces*, 2015, **7**, 15840–15847.

31 K. B. Xu, Q. L. Ren, Q. Liu, W. Y. Li, R. J. Zou and J. Q. Hu, *RSC Adv.*, 2015, **5**, 44642–44647.

32 W. B. Fu, C. H. Zhao, W. H. Han, Y. Liu, H. Zhao, Y. F. Ma and E. Q. Xie, *J. Mater. Chem. A*, 2015, **3**, 10492–10497.

33 L. Y. Niu, Y. D. Wang, F. P. Ruan, C. Shen, S. Shan, M. Xu, Z. K. Sun, C. Li, X. J. Liu and Y. Y. Gong, *J. Mater. Chem. A*, 2016, **4**, 5669–5677.

34 D. Z. Kong, W. N. Ren, C. W. Cheng, Y. Wang, Z. X. Huang and H. Y. Yang, *ACS Appl. Mater. Interfaces*, 2015, **7**, 21334–21346.

35 C. Zhou, Y. W. Zhang, Y. Y. Li and J. P. Liu, *Nano Lett.*, 2013, **13**, 2078–2085.

36 M. L. Yan, Y. D. Yao, J. Q. Wen, L. Long, M. L. Kong, G. G. Zhang, X. M. Liao, G. F. Yin and Z. B. Huang, *ACS Appl. Mater. Interfaces*, 2016, **8**, 24525–24535.

37 A. Laheaar, P. Przygocki, Q. Abbas and F. Beguin, *Electrochem. Commun.*, 2015, **60**, 21–25.

38 W. Kong, C. C. Lu, W. Zhang, J. Pub and Z. H. Wang, *J. Mater. Chem. A*, 2015, **3**, 12452–12460.

39 T. T. Chen, Y. Fan, G. N. Wang, Q. Yang and R. X. Yang, *RSC Adv.*, 2015, **5**, 74523–74530.

40 H. Peng, G. F. Ma, K. J. Sun, J. J. Mu, H. Wang and Z. Q. Lei, *J. Mater. Chem. A*, 2014, **2**, 3303–3307.

41 J. Hu, M. C. Li, F. C. Lv, M. Y. Yang, P. P. Tao, Y. G. Tang, H. T. Liu and Z. G. Lu, *J. Power Sources*, 2015, **294**, 120–127.

42 D. P. Cai, D. D. Wang, C. X. Wang, B. Liu, L. L. Wang, Y. Liu, Q. H. Li and T. H. Wang, *Electrochim. Acta*, 2015, **151**, 35–41.

43 T. Brousse, D. Belanger and J. W. Long, *J. Electrochem. Soc.*, 2015, **162**, A5185–A5189.

44 Y. Liu, X. Y. Cai, B. F. Luo, M. Yan, J. H. Jiang and W. D. Shi, *Carbon*, 2016, **107**, 426–432.

45 Z. S. Wu, D. W. Wang, W. Ren, J. Zhao, G. Zhou, F. Li and H. M. Cheng, *Adv. Funct. Mater.*, 2010, **20**, 3595–3602.

46 K. B. Xu, X. J. Huang, Q. Liu, R. J. Zou, W. Y. Li, X. J. Liu, S. J. Li, J. M. Yang and J. Q. Hu, *J. Mater. Chem. A*, 2014, **2**, 16731–16739.

47 N. Jabeen, Q. Y. Xia, M. Yang and H. Xia, *ACS Appl. Mater. Interfaces*, 2016, **8**, 6093–6100.

48 R. J. Zou, Z. Y. Zhang, M. F. Yuen, J. Q. Hu, C. S. Lee and W. J. Zhang, *Sci. Rep.*, 2015, **5**, 7862.

49 Y. F. Yang, D. Cheng, S. J. Chen, Y. L. Guan and J. Xiong, *Electrochim. Acta*, 2016, **193**, 116–127.

50 W. J. Ren, D. Guo, M. Zhuo, B. K. Guan, D. Zhang and Q. H. Li, *RSC Adv.*, 2015, **5**, 21881–21887.

51 K. B. Xu, R. J. Zou, W. Y. Li, Q. Liu, X. J. Liu, L. An and J. Q. Hu, *J. Mater. Chem. A*, 2014, **2**, 10090–10097.

52 D. Cheng, Y. F. Yang, J. L. Xie, C. J. Fang, G. Q. Zhang and J. Xiong, *J. Mater. Chem. A*, 2015, **3**, 14348–14357.

53 L. Mei, T. Yang, C. Xu, M. Zhang, L. B. Chen, Q. H. Li and T. H. Wang, *Nano Energy*, 2014, **3**, 36–45.

54 R. Li, S. L. Wang, Z. C. Huang, F. X. Lu and T. B. He, *J. Power Sources*, 2016, **312**, 156–164.

55 L. J. Han, P. Y. Tang and L. Zhang, *Nano Energy*, 2014, **7**, 42–51.

56 Q. Ke, M. Zheng, H. Liu, C. Guan, L. Mao and J. Wang, *Sci. Rep.*, 2015, **5**, 13940.